Biofabrication

International Society for Biofabrication

**ACCEPTED MANUSCRIPT**

# Engineering a dynamic three-dimensional cell culturing microenvironment using a “sandwich” structure-liked microfluidic device with 3D printing scaffold

To cite this article before publication: Laiqian Ding *et al* 2022 *Biofabrication* in press https://doi.org/10.1088/1758-5090/ac8a19

# Engineering a dynamic three-dimensional cell culturing microenvironment using a "sandwich" structure-liked microfluidic device with 3D printing scaffold

**Laiqian Ding[1], Chong Liu[1,3], Shuqing Yin[1], Zhanwei Zhou[4], Jing Chen[4], Xueting Chen[4], Li Chen[1], Dazhi Wang[1], Bo Liu[5], Yuanchang Liu[2], Juan Wei[6*], Jingmin Li[1*]**

*[1]Key Laboratory for Micro/Nano Technology and System of Liaoning Province, Dalian University of Technology, Dalian, China*

*[2]Department of Mechanical Engineering, University College London, London, UK, WC1E 6BT*

*[3]Key Laboratory for Precision and Non-traditional Machining Technology of Ministry of Education, Dalian University of Technology, Dalian, China*

*[4]Beijing Spacecrafts Co., Ltd., Beijing, China*

*[5]Department of Biomedical Engineering, Dalian University of Technology, Dalian, China*

*[6]Centre for Advanced Laser Manufacturing (CALM), School of Mechanical Engineering, Shandong University of Technology, Zibo, China*

***Corresponding Email: jingminl@dlut.edu.cn; weijuan@sdut.edu.cn**

**Abstract**

Most of *in vivo* tissue cells reside in 3D extracellular matrix (ECM) with fluid flow. To better study cell physiology and pathophysiology, there has been an increasing need in the development of methods for culturing cells in *in vivo* like microenvironments with a number of strategies currently being investigated including hydrogels, spheroids, tissue scaffolds and very promising microfluidic systems. In this paper, a "sandwich" structure-liked microfluidic device integrated with a 3D printing scaffold is proposed for three-dimensional and dynamic cell culture. The device consists of three layers, i.e. upper layer, scaffold layer and bottom layer. The upper layer is used for introducing cells and fixing scaffold, the scaffold layer mimicking ECM is used for providing 3D attachment areas, and the bottom layer mimicking blood vessels is used for supplying dynamic medium for cells. Thermally assisted electrohydrodynamic jet (TAEJ) printing technology and microfabrication technology are combined to fabricate the device. The flow field in the chamber of device is evaluated by numerical simulation and particle tracking technology to investigate the effects of scaffold on fluid microenvironment. The cell culturing processes are presented by the flow behaviours of inks with different colors. The densities and viabilities of HeLa cells are evaluated and compared after 72 h of culturing in the microfluidic devices and 48-well plate. The dose-dependent cell responses to doxorubicin hydrochloride (DOX) are observed after 24 h treatment at different concentrations. These experimental results, including the evaluation of cell proliferation and *in vitro* cytotoxicity assessment of DOX in the devices and plate, demonstrate that the presented microfluidic device has good biocompatibility and feasibility, which have great potential in providing native microenvironments for *in vitro* cell studies, tissue engineering and drug screening for tumor therapy.

**Keywords:** three-dimensional cell culturing model; dynamic; microfluidic; 3D printing scaffold; drug treatment

## 1. Introduction

Cell is the basic unit of life in all forms of living organisms and cell researches based upon *in vitro* cell culture have significance in exploring the inducement of diseases and developing drugs [1,2]. Two-dimensional cell culture techniques, in which cells are grown on a flat substrate such as dishes or plates, are typical *in vitro* cell culture methods [3,4]. However, most of cells reside in complex three-dimensional microenvironments, where complex factors, such as cell-ECM interaction, cell-cell interaction, biochemical factors, and shear stress induced by fluid flow, exist. [5-8]. It has been demonstrated that native in vivo cell characteristics can be well maintained when cells are being cultured in an in vitro environment by employing a three dimensional culturing model [9-11].

A variety of techniques have been used to construct bioengineered 3D culturing models with the cell encapsulation being one of the dominant methods. Naturally derived or synthetic hydrogels are normally adopted to build 3D models [12-14]. The hydrogels have the advantages of high water content and biocompatibility. However, for synthetic hydrogels, the degradation byproducts as well as the degradation rate are difficult to be controlled to match the proliferation rate of cells and provide sufficient culturing space for cells. Also, for naturally derived hydrogels, unquantified impurities, and undesired immunogenicity are additional challenges for constructing the 3D environment [15]. Alternatively, engineering microporous structures on biocompatible polymer materials can be directly designed by using chemical or physical methods. For example, solvent casting/particle leaching [16], freeze-drying [17,18] and gas foaming [19] can be used to construct the microporous structure to mimic ECM. However, when cells are implanted into the microporous structures, an uneven distribution can be potentially induced because of the limited controllability of the porous structures. In addition, the mass transportation in such porous structures dominated by passive diffusion are often insufficient.

To address the issue of limited controllability, 3D printing technology has been proposed to provide a precise porous control [20-22]. In general, the polymer filaments can be precisely stacked into 3D structures with fine surface quality and a uniform cells distribution can be achieved inside the printing tissue scaffold. The 3D printing technology has also been used to fabricate cell-laden droplets for 3D culturing [23,24]. However, the culturing models are still static with the absence of mimicking crucial *in vivo* parts such blood vessels, resulting in the insufficiency of nutrition delivery and the accumulation of cell metabolites. To address such an issue, the microfluidic technology has been widely adopted in recent decades [25-27]. It is used to generate microwells using micromolding on microfluidic chips to provide a simple, confined 3D space for accelerating cell aggregation and directing cell spheroid formation [28,29]. Besides, object regions inside microfluidic chips filled with cell-laden hydrogels or 3D bioprinting cell clusters are used for 3D dynamic cell culture [30-33]. For example, liver on a chips with 3D constructs were developed for in vitro drug toxicity assessment and their dose-dependent drug responses verified their broad prospects of predicting in vivo hepatotoxicity and developing high throughput drug screening [32,33]. However, the adhesion strength between hydrogels or cell clusters and microfluidic chips is relatively weak, making the constructed 3D culturing models subject to potential structure deformation and unstability due to the impact of fluid flow. In addition, hydrogels with microfluidic channels mimicking blood vessels are also designed [34-36]. The creation of microfluidic channels in hydrogels greatly improves mass transportation by convection and diffusion. Nevertheless, similar to the disadvantages of conventional hydrogel based 3D cell culturing methods, the space of cells encapsulated in hydrogels in the microfluidic chip is still constrained.

In this work, a new method of building an *in vitro* 3D culturing model mimicking ECM and microcirculation is presented. The designed device has a structure of "sandwich", including upper layer, scaffold layer and bottom layer. By using the engineered device, the implanted cells can reside in the 3D

model with enhanced stability and sufficient growth space. Based on a convection-dominant mechanism, the created environment is capable of providing a smooth supply of nutrition and has better resemblance to *in vivo* living environment. More specifically, 3D tissue scaffold providing enough support for cell growth and implantation has been printed using thermally assisted electrohydrodynamic jet (TAEJ) printing technology. The size of the printed filaments can be controlled in the scale of ECM or living cells. Micromolding technology is used to fabricate microchannels such that the mechanism of blood vessels for providing nutrients and removing metabolic wastes can be mimicked. The hierarchical microchannels are designed to provide redundant paths to transport medium to cells allowing a stable and homogeneous nutrition supply by convection and diffusion. Within the "sandwich" structure, the scaffold layer is tightly integrated into the microfluidic chamber by using oxygen plasma treatment. Importantly, the stability of the structure of scaffold is improved by designing flexible fixed feet on the microfluidic plate to fix the scaffold in the form of interference fit to prevent deformation from flushing by fluid flow. Numerical simulation with two computational fluid dynamics (CFD) models and particle tracking experiment are used to evaluate the ability of scaffold to stabilize the flow field in the device. To validate the operability of microfluidic device, the flow behaviours inside the device are demonstrated by inks with different colors. HeLa cells are cultured in three-dimension in the microfluidic device under continuous medium supply, and are compared with the cells cultured in two-dimension in the 48-well plate and the device without scaffold. *In vitro* cytotoxicity assessment of DOX in the devices and plate are performed for the verification of device functionality.

## 2. Materials and methods

### 2.1. Materials and reagents

The polydimethylsiloxane (PDMS) used here was purchased from Dowing Corporation (Midland-Michigan, USA). The polycaprolactone (PCL) ink was prepared by dissolving 10.3 wt % of PCL (Mw = 800 000, Yuanye Bio-Technology Co., Ltd, China) particles into acetic acid (Adamas Reagent Co., Ltd, China) and mixing for 50 min at 80 °C. The polyvinyl pyrrolidone (PVP) ink was prepared by dissolving 12.6 wt% of PVP powders into ethanol, adding 0.43 wt % of polyethylene glycol (PEG, Mw=800, Kemiou Chemical Reagent Co., Ltd, China), mixing for 8 min at 50 °C, then adding 1.7 wt % of Triton X-100 and mixing for 10 min. The PCL ink and PVP ink were mixed for 20 min at 25 °C to form PCL/PVP composite biopolymer ink. The polystyrene (PS) microbeads with a nominal diameter of 1.33 μm purchased from Sphere Scientific Corporation (Hubei, China) were selected as the tracking particles to evaluate the flow field in the microfluidic device. The blue and red inks which represented HeLa cell suspension and culture medium respectively for simulating cell culturing process were purchased from Shanghai Hero Corporation (Shanghai, China). The culture medium used for experiments consists of 89% Dulbecco's Modified Eagle Media, 10% fetal bovine serum, 1% penicillin and streptomycin (Gibco, USA). The fibronectin (Roche Diagnostics, Indianapolis, USA) was used to improve the biocompatibility of microenvironment. HeLa cells were purchased from Cell Bank of the Chinese Academy of Sciences (Shanghai, China). The cells were stained using FDA/PI (live/dead, Solarbio, Beijing, China). Doxorubicin hydrochloride (DOX) and dimethyl sulfoxide (DMSO) were purchased from Aladdin Reagent Co., Ltd (Shanghai, China). Cell Counting Kit-8 (CCK-8) was purchased from Beyotime Biotechnology Ltd (Shanghai, China).

### 2.2. Design of the "sandwich" structure-liked microfluidic device

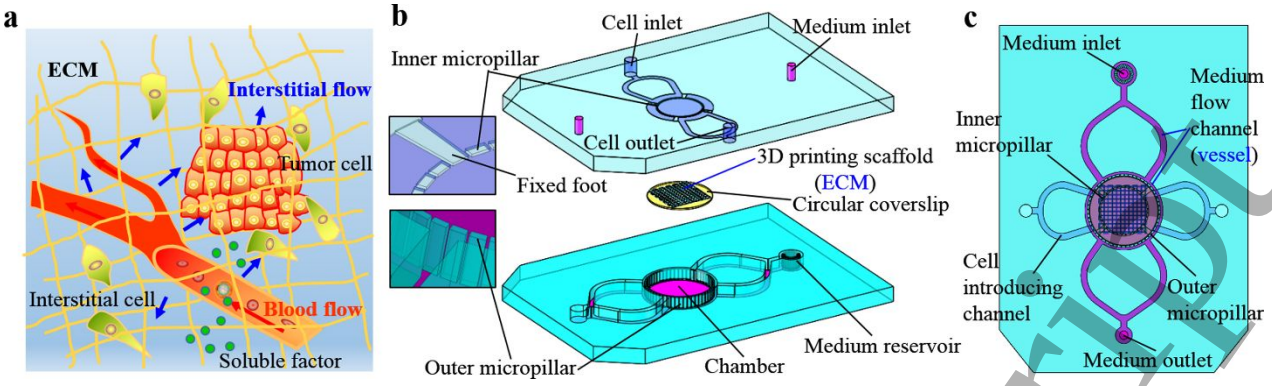


Fig. 1 Design of the microfluidic device. (a) Schematic of the cellular *in vivo* microenvironments. (b) Schematic of the designed microfluidic device consisting of upper layer, scaffold layer and bottom layer. (c) Top view of the integrated microfluidic device.

*In vivo* cells reside in a complex 3D microenvironment, where factors such as soluble factors, cell-cell contacts, cell-ECM interactions and shear stresses induced by fluid flow (as shown in Fig. 1a) exist. Blood vessels transport oxygen and nutrients to tissue cells. Interstitial flow existing in the tissue interstitium helps move nutrients, wastes, and soluble factors to and from cells that may be distant from blood capillaries. Inspired by such a 3D microenvironment of *in vivo* cells, a "sandwich" structure-liked microfluidic device that is able to provide 3D tissue scaffold and dynamic fluid for cell culture has been designed. The device consists of three layers, i.e. upper layer, scaffold layer and bottom layer (as shown in Fig. 1b).

The upper layer is a plate with a medium inlet, a medium outlet, a cell inlet, cell introducing channels, a cell outlet and inner micropillars and is designed for introducing cells and fixing the scaffold layer. The depths of the inlets, outlets and channels are 70 μm. The inner micropillars are composed of a circular array of micropillars and four fixed feet with a height of 120 μm. The inner micropillars are bulges of the upper plate, which are used for fixing the scaffold. The circumferential width of microgaps between inner micropillars is 40 μm, which is larger than the sizes of cells, making the microgaps capable of providing smooth paths for introducing cells. Due to the square shape of scaffold used in this paper, four fixed feet were designed to fix the four corners of the scaffold and to guide the flow of cell suspension.

The scaffold layer consisting of a 3D printed scaffold and a circular coverslip was implanted in the bottom layer and fixed by the upper layer. The circular coverslip is a 48-well plate cell slide with the diameter of 8000 μm and thickness of 130 μm ($D_c$). Before printing the scaffold, the coverslip was cleaned by acetone, ethanol and deionized water in sequence. The 3D printed scaffold was inscribed in the circular coverslip according to the designed printing program. Cells infused from the cell introducing channels could settle on the 3D printed scaffold.

The bottom layer is a substrate with a medium reservoir, medium flow channels, outer micropillars, a chamber and a waster reservoir. The medium reservoir contains a circular array of micropillars to filter the impurities in culture medium. The medium flow channels are two-stage bifurcation channels. The hydraulic diameters of the bifurcated channels obey Murray's law, which mimics the structural arrangement of blood vessels. The circumferential width of microgaps between outer micropillars is also 40 μm. The multi-microgaps can provide multiple flow paths for culture medium flowing into the scaffold, which has been demonstrated to be useful for constructing uniform and stable flow fields [37,38]. The chamber with a diameter of 8020 μm was designed to locate the circular coverslip. The depths of the medium reservoir, medium flow channels, microgaps between outer micropillars, chamber and waster reservoir are 200 μm. Fig. 1c shows the integrated microfluidic device and the corresponding positions of structures on different layers. The size of the integrated microfluidic device is 40 mm × 29 mm × 3 mm.

## 2.3. Fabrication of the microfluidic device

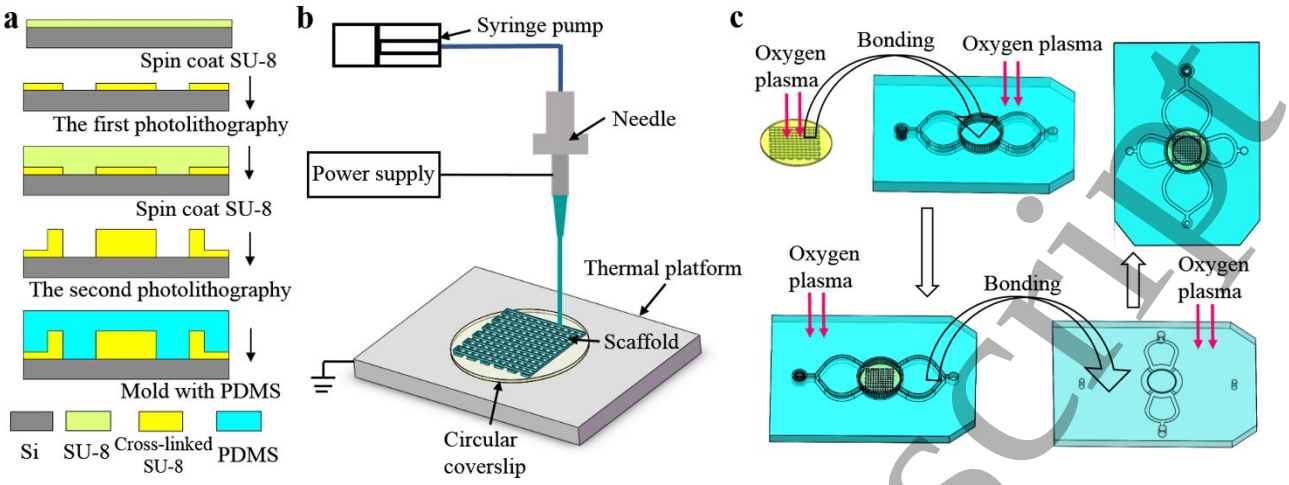


Fig. 2 Schematic of fabrication processes of the microfluidic device. (a) Fabrication process of the upper PDMS layer and bottom PDMS layer. (b) Schematic diagram showing the TAEJ printing process. (c) Bonding process of the whole device.

The upper layer and bottom layer of the microfluidic device were fabricated with PDMS by replicating structures on the masters (as shown in Fig. 2a). The masters were prepared by spin-coating the SU8-2035 negative photoresist (Microchem Corp., Newton, MA, USA) onto silicon wafers and patterned by photolithography. Twice photolithography was used to fabricate the raised inner micropillars on upper layer. After silanization treatment of masters, the PDMS base and curing agent were mixed thoroughly (10:1 by mass), degassed under vacuum, and poured onto the masters. Then the masters were put in self leveling drying baker and the PDMS was oven-cured (80 °C, 1 h). After cooling, the PDMS layers were gently peeled from the masters and trimmed to the required size. Inlet and outlet holes were punched out of the PDMS to connect the tubes for introducing medium.

The scaffold layer was fabricated by TAEJ printing technology (as shown in Fig. 2b). The printing processes were established according to the protocols described in our previous work [39]. First, the composite biopolymer ink of PCL/PVP was prepared and followed by the process of delivering the PCL/PVP composite biopolymer ink into the needle using a syringe pump. Then, the thermal radiation produced by thermal platform was applied on the composite ink for rapid solvent evaporation. In this process, the solvents with low boiling point, such as ethyl alcohol and acetic acid, were evaporated quickly, leading to an increase in the viscosity of composite biopolymer ink. In order to generate an electric shearing force and induce the biopolymer ink to form a jet, an appropriate voltage of 800 V was applied between the needle and the thermal platform. This stable and controllable fine jet enables to directly write high-resolution biopolymer structures with the help of X-Y-Z movement stage.

Finally, the whole device was bonded using oxygen plasma treatment (as shown in Fig. 2c). The scaffold layer and bottom layer were treated by oxygen plasma (35 W, 50 s) simultaneously. The side without scaffold of circular coverslip was put into the chamber on the bottom layer after oxygen plasma treatment. By applying a gentle pressing force, the scaffold layer was reversibly bonded on the bottom layer. Then the bonding plate and upper layer were placed into the oxygen plasma ashing apparatus for 50 s simultaneously. The upper layer and bonding plate were aligned using the visual alignment equipment and bonded irreversibly [38].

## 2.4. Numerical simulation

To investigate the effect of 3D printing scaffold on the flow field in the chamber of microfluidic device, two 2D-CFD models based on laminar Poiseuille flow were developed by using COMSOL Multiphysics 5.3 (Burlington, MA). Thereinto, the model without scaffold was used as the control group. The scaffold in the other was set as a porous media domain of which the porosity was approximately 0.8 calculated following the previous theoretical method [40] dependent of three parameters including fiber diameter, fiber spacing and layer thickness. Water at 20 °C was selected as the fluid material, and the scaffold permeability was about $4.2\times10^{-9}$ $m^2$ determined by Darcy's law [41]. For both models, Navier-Stokes equation with no slip boundary condition was employed to study the flow velocity and flow field distribution in the chamber of device, and 2 μL/min was set as the flow rate of inlet.

2.5. Evaluation of flow field in the microfluidic device

As described previously [37], particle tracking technology was used to evaluate the condition of flow field in the chamber of microfluidic device with/without scaffold. First, the PS microbeads with an initial density of 0.95 ~ 1.05 g/$cm^3$ were diluted with deionized water to obtain a 0.01% suspension. Second, the microbead suspension was perfused into the device by a syringe pump (Harvard PHD-Ultra, USA) with a flow rate of 2 μL/min and a 5 mL syringe which was connected to the medium inlet with a 0.8 mm interior diameter silicone tube. Third, the movements of PS microbeads reflecting the flow condition in the chamber were recorded by an inverted microscope (Olympus IX71, Japan) with a CCD camera at an interval of 50 ms after the flow reached a steady state. Finally, the images were dealt with Image-Pro Plus 6.0 (Media Cybernetics Inc., USA) to draw the trajectories of PS microbeads and calculate their average velocities in the chamber of device.

2.6. Cell culture

HeLa cells were cultured to verify the biocompatibility and feasibility of the microfluidic device. HeLa cells in 48-well plate covered with circular glass and in the microfluidic device without scaffold were used as comparisons respectively. Cell culturing processes are as follow. First, the microfluidic devices and silicone tubes were washed with 75% ethanol and deionized water, dried and sterilized by UV light for at least 1 h. Before introducing cells, the devices were filled with culture medium to remove any gas. Second, the devices were coated with 5 μg/mL fibronectin and incubated at 37 °C for 6 h to increase the attachment of cells. Third, after removing the surplus proteins by infusing culture medium, 20 μL HeLa cell suspension at a concentration of $1\times10^6$ cells/mL was introduced into the device from the cell introducing channel by the syringe pump with a flow rate of 100 μL/min. 200 μL cell suspension at a concentration of $1\times10^5$ cells/mL was introduced into 48-well plate. Then the cells were cultured in static in a 5% $CO_2$ incubator at 37 °C to increase the attachment of cells. After culturing for 6 h, the perfusion of the culture medium to microfluidic device was initiated and completed inside the incubator. The device was connected to a perfusion system containing 0.8 mm interior diameter silicone tubes, a syringe pump with flow rate of 2 μL/min and a 5 mL syringe. The culture media in the syringe and 48-well plate were changed every 24 h.

The cells were investigated under the inverted microscope (Olympus IX73, Japan) every 24 h. The cells were stained by FDA/PI (live/dead) for 30 min at 37 °C after culturing for 72 h. Live cells were labeled as green and dead cells were labeled as red under the fluorescence microscope. The cell viability and final normalized cell density were estimated by dealing the fluorescence images with Image-Pro Plus 6.0. The spatial distributions of HeLa cells in devices and plate were investigated by a laser scanning confocal microscope (Olympus FV1000, Japan) after 72 h of culturing. The scanning step size of all groups was set to 0.5 μm for recording the slices of z-stacking, and the confocal images were processed with Image-Pro

Plus 6.0 software to reconstruct cell distribution. To evaluate cell morphology in devices and plate, cell aspect ratio was calculated by dividing cell length by cell width. The cell length and width in fluorescence images of all groups were measured with Image-Pro Plus 6.0 software, and 100 cells were randomly selected in each group.

### 2.7. Drug (DOX) treatment

A mother solution of 1 mM DOX was prepared in the DMSO, and then it was diluted with the culture medium to reach the final concentration of 1, 5, 10, 20, and 40 μM respectively. The calibration experiment was carried out by measuring the absorbance of the above-mentioned DOX solutions with known concentrations using a UV-vis spectrophotometer (JENWAY 7305, UK) at 485 nm, and the derived standard curve (Fig. S1) was obtained. According to the previous reports [42,43], DOX concentrations of 1 and 10 μM that cover a range from no significant cytotoxicity to acute cytotoxicity were chosen for the subsequent experiments to assess the dose-dependent responses to DOX. The drug treatment for HeLa cells of all groups was performed after culturing of 72 h. For 2D static conditions in plate, HeLa cells were exposed to the fresh culture medium containing DOX with different concentrations. For dynamic conditions in devices, the same culture medium was perfused into the chamber of microfluidic chip through the inlet by a syringe pump with a flow rate of 2 μL/min. Cells with no treatment were used as controls in each group.

In order to investigate the DOX accumulation in plate and devices, DOX concentrations in the metabolic wastes collected from the plate and the outlet of microfluidic chips were determined by measuring the absorbance and assigning to the DOX standard curve after 24 h treatment. The relative changes in DOX concentration of metabolic wastes compared with the initial concentration were calculated as: $(c_i - c)/c_i \times 100\%$, where $c_i$ refers to the initial concentration of DOX in the fresh culture medium, and $c$ refers to the final DOX concentration in the metabolic wastes collected from the plate and the outlet of devices [42]. According to the relative changes in DOX concentration, the amount of DOX accumulated in HeLa cells was calculated by subtracting the residual DOX in the waste from the total DOX amount in the initial culture medium [42]. To compare the dose-dependent responses to DOX in different culturing conditions, the CCK-8 was used to assess the cytotoxicity of DOX quantitatively after 24 h treatment. A working solution was prepared by mixing CCK-8 and culture medium containing DOX with different concentrations (1:10 v/v). For 2D static conditions in the 48-well plate, 240 μL working solution was added to each well of plate and then incubated for 2 h. For dynamic conditions in devices, the working solution was perfused into the chamber of microfluidic chip through the inlet by a syringe pump with a flow rate of 2 μL/min for 2 h. After incubation, the solutions collected from the plate and devices were aspirated and added to a 96-well plate, and the absorbance at 450 nm was measured by using a microplate reader (TECAN INFINITE E PLEX, Switzerland). The cell viability reflecting the cytotoxicity of DOX was calculated as: $(A_2 - A_0)/(A_1 - A_0) \times 100\%$, where $A_0$ refers to the absorbance of the blank control with culture medium and CCK-8 (without cells), $A_1$ refers to the absorbance of the group with cells and CCK-8 (without DOX), and $A_2$ refers to the absorbance of the group with cells, DOX and CCK-8 [44]. Besides, HeLa cells after DOX treatment with different concentrations in devices and plate were stained by FDA/PI (live/dead) for visualization of cell responses to DOX including the changes in cell viability and morphology.

### 2.8. Statistical analysis

Data were presented as mean ± standard deviation (SD) using Origin software (version 2019b, OriginLab, USA). Mann-Whitney u-test and two-tailed unpaired Student's t-test were used to compare the data and $p < 0.05$ was taken as the level of significance.

## 3. Results and discussion

### 3.1. Structures of the fabricated device

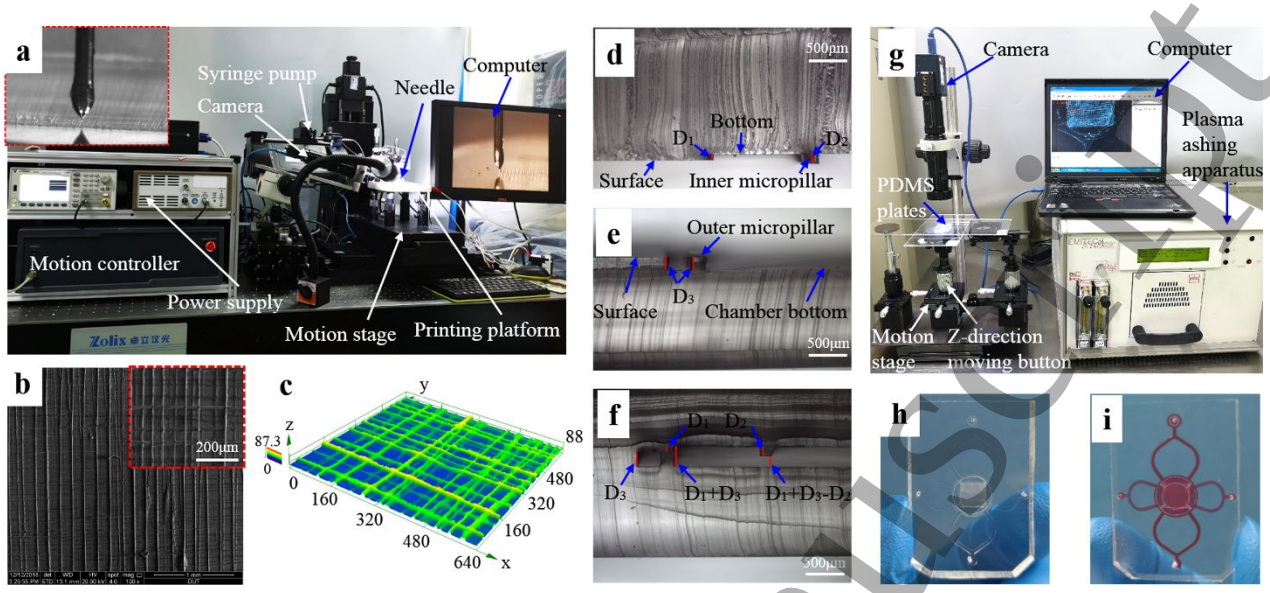


Fig. 3 The object of the fabricated structures. (a) Equipment used for printing the 3D PCL/PVP scaffold. (b) SEM images of the 3D printing scaffold. (c) 3D profile of the scaffold. (d) Sectional image of the upper PDMS layer. (e) Sectional image of the bottom PDMS layer. (f) Sectional image of the bonded device. (g) Equipment used for bonding the three layers. (h) The object of the whole device. (i) Image of the device filled with red ink.

The TAEJ printing process mainly uses the electrohydrodynamic effect on composite biopolymer ink at the outlet of the needle to form jet, combined with rapid solvent evaporation on this jet. Fig. 3a shows the formation of the semisolid biopolymer cone-jet during the printing process. A needle with an inner diameter of 50 μm was used in this experiment. During the printing process, the temperature of thermal platform, the applied voltage, the flow rate of syringe pump and the movement speed of motion stage were set at 55 °C, 800 V, $6 \times 10^{-11}$ $m^3/s$, and 3 mm/s, respectively. The 3D PCL/PVP scaffold was printed on a circular glass substrate matching with the 48-well plate. Six layers were printed in a way that one layer was printed as the X-direction with its adjacent layer being printed in the Y-direction. The plan size of the scaffold is 5600 × 5600 μm and the distance between two adjacent filaments is set as 80 μm. Fig. 3b shows the 3D structure printed layer-by-layer using TAEJ printing technology. The average width of the scaffold filaments is about 12 μm and the average distance between two adjacent filaments is about 70 μm for this scaffold. Fig. 3c shows the 3D profile of the scaffold and the height of the printed scaffold ($D_s$) is about 40 μm. It can be seen from the 3D profile that the scaffold exhibits uniform and smooth features.

The upper layer and bottom layer were fabricated with PDMS by replicating the structures on SU-8 molds. Fig. 3d shows the key structures of upper layer. The distance between surface and bottom is 70 μm ($D_1$) and the height of inner micropillars is 120 μm ($D_2$). It can be seen that the inner micropillars are bulge of the upper plate and the heights of the bulges are 50 μm ($D_2$ - $D_1$). Fig. 3e shows the key structures of the bottom layer. The depth of chamber is equal to the height of outer micropillar, which is 200 μm ($D_3$). The aligned structures of upper layer and bottom layer are shown in Fig. 3f. It can be seen the hanging heights of inner micropillar and fix feet relative to the chamber bottom of bottom layer is 150 μm ($D_1$ + $D_3$ - $D_2$), which is smaller than the thickness of scaffold layer, 170 μm ($D_s$ + $D_c$) and larger than the thickness of circular coverslip, 130 μm ($D_c$). In this way, the scaffold can be fixed by the flexible PDMS fixed feet through interference fit. As a result, the stability of the scaffold structure is improved by preventing

deformation from flushing by fluid flow.

To align these three layers of microfluidic device, an alignment bonding equipment has been assembled (as shown in Fig. 3g). The processes of the layer alignment can be summarized as follows. First, after being treated by oxygen plasma, one PDMS piece was put on the lower surface of the up plate with another PDMS piece being put on the upper surface of the bottom support plate. Because of the feature of the PDMS piece being able to attach on the surface of glass and bond reversibly by Van der Waals' force, the PDMS piece attached on the lower surface of the up plate would not drop off. Then, aligning the two PDMS pieces in Z-direction by adjust the motion stage. Last, rotating the Z-direction moving button to push the bottom PDMS piece to the upper PDMS piece, and the two PDMS pieces were being bonded irreversibly (as shown in Fig. 3h). The bonded device was filled with red ink (Fig. 3i), which shows that the flow condition inside the device is good.

3.2. Effects of scaffold on the flow field in the device

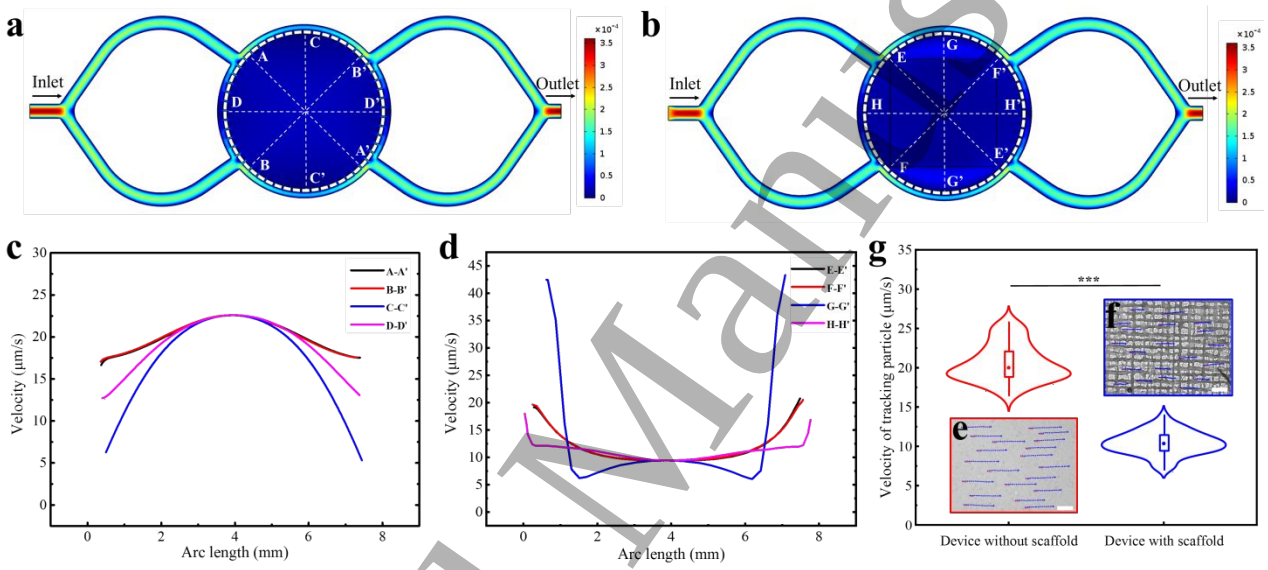


Fig. 4 The condition of flow fields and effects of 3D printing scaffold on the flow field in the chamber of microfluidic device. (a) Steady-state simulation result of velocity field in the chamber without scaffold; four cross lines are plotted and uniformly distributed in the circumferential direction of the chamber; the units of color legend is m/s. (b) Steady-state simulation result of velocity field in the chamber with scaffold; the square area in the chamber represents the scaffold; four cross lines are plotted and uniformly distributed in the circumferential direction of the chamber; the units of color legend is m/s. (c) The velocity profile along the cross-line A-A', B-B', C-C' and D-D'. (d) The velocity profile along the cross-line E-E', F-F', G-G' and H-H'. (e) Trajectories of PS microbeads in the chamber without scaffold; blue lines represent the trajectories of the selected microbeads. (f) Trajectories of PS microbeads in the chamber with scaffold; blue lines represent the trajectories of the selected microbeads. (g) The velocity of tracking particles in the chamber of device; Mann-Whitney *u*-test is used for analysis of the data; *** indicates statistical significance of $P < 0.001$ ($n = 80$). The scale bar is 100 μm.

To study the effects of 3D printing scaffold on the condition of flow field in the device, two CFD models with the same boundary and inlet condition have been developed by COMSOL Multiphysics 5.3, and the steady-state simulation results of velocity field are shown in Fig. 4a and Fig. 4b, respectively. Qualitatively, it is observed that the flow velocity in the control chamber (Fig. 4a) is apparently faster than that in the scaffold area (Fig. 4b) by comparing the gradation of color. In order to make a quantitative analysis for the flow velocity and flow field distribution in the chamber, four cross lines are plotted in either of chambers.

Fig. 4c shows the velocity curves along the cross-line A-A', B-B', C-C' and D-D'. These parabola-liked curves indicate that the distribution of flow field in the chamber is obviously nonuniform. The maximum velocity, up to 22.6 μm/s, occurs in the center of chamber. On the contrary, the distribution of flow field in the scaffold area is more uniform than that of the control group according to the relatively smooth curves along the cross-line E-E', F-F', G-G' and H-H'(as shown in Fig. 4d). And the velocity in the geometric center of scaffold that is about half that in the center of the control chamber is generally slower than that in the surrounding area of scaffold except in the direction of cross-line G-G'. It is demonstrated that the scaffold can stabilize the flow field in the chamber to a certain extent.

The flow behavior in the device is further revealed by the trajectories of PS microbeads in the chamber. Four positions around the center of chamber are stochastically selected and recorded by a CCD camera, and the average velocities of 20 PS microbeads that are uniformly distributed in every position are chosen to represent the velocities in the chambers (as shown in Fig. 4e and Fig. 4f). The length of blue trajectories indicates that the average velocities in the control chamber are faster than those in the scaffold area. Fig. 4g shows the violin plot of average tracking particle velocities in different devices. The red and blue point denotes the median of velocity samples that is about 20.0 μm/s and 10.4 μm/s, respectively. It is also observed that the height of the red violin plot (device without scaffold) is greater than that of the blue (device with scaffold), which demonstrates that former has a more dispersed distribution of velocity and the scaffold can provide a more uniform flow microenvironment for cell culture. The experimental results are in accordance with the analysis of numerical simulation.

3.3. Cell culturing process simulated by the flow of inks

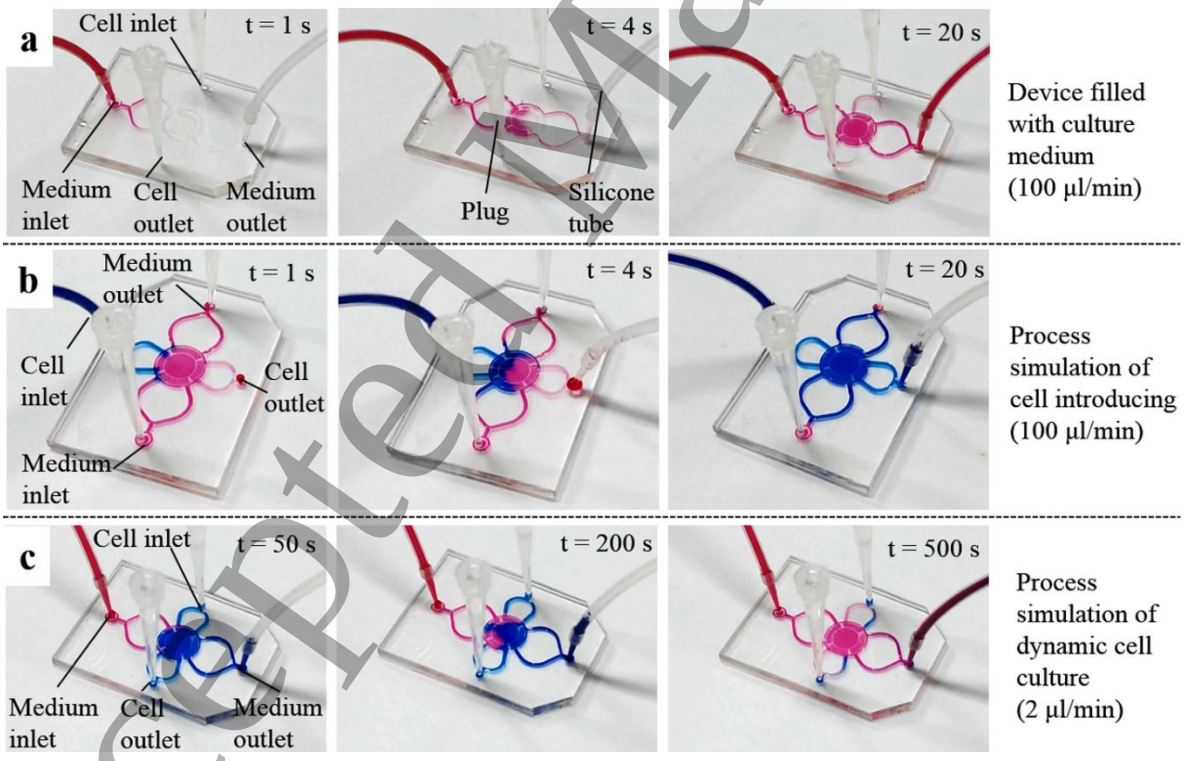


Fig. 5 Simulation of cell culturing process. (a) The simulation of process that the microfluidic device is full with culture medium. (b)The simulation of cell introducing process. (c) The simulation of culture medium infusing process.

In order to present the process of cell culturing, the flow behaviours of inks with different colors have been investigated. First, the device was filled with culture medium (red ink) to remove gas before introducing HeLa cell suspension (blue ink). The cell inlet and cell outlet were blocked by plugs and culture medium

was infused into the device with a flow rate of 100 μL/min by connecting the medium inlet to a syringe pump (as shown in Fig. 5a). It can be seen that the device is filled with red ink after infusing for 20 s. Then, cell suspension (blue ink) was introduced into the device from the cell inlet by a syringe pump with a flow rate of 100 μL/min and the redundant cell suspensions spilled from cell outlet. The medium inlet and medium outlet were blocked by plugs (as shown in Fig. 5b). The result shows that the culture chamber is filled with blue ink after infusing for 20 s. In order to avoid cell settlement, the infusing time was reduced by opening the cell outlet. The silicon tube was insert into cell outlet until the spill of cell suspension (blue ink) and the infusion was stopped. After standing in static for 6 h, the infusion of culture medium was started by connect the medium inlet to a syringe pump with a flow rate of 2 μL/min. The cell inlet and cell outlet were blocked (as shown in Fig. 5c). The result shows that the device is full with red ink after infusing for 500 s, which indicates that the culture chamber is filled with culture medium and the waste medium flows out from medium outlets.

### 3.4. HeLa cells cultured in the devices and plate

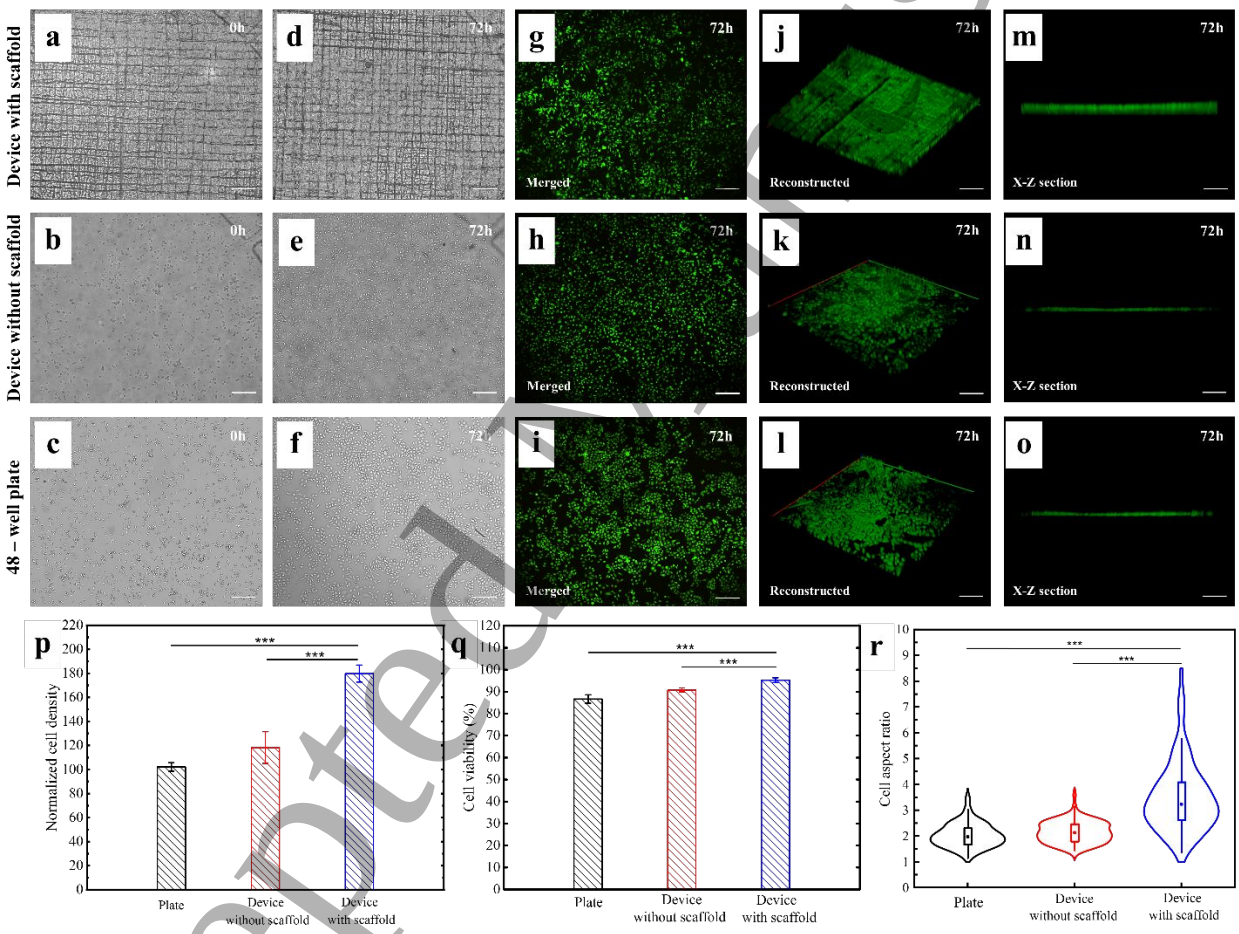


Fig. 6 HeLa cells grow inside the microfluidic devices and plate. (a-c) HeLa cells cultured in the microfluidic device with scaffold, device without scaffold and 48-well plate covered with circular glass at 0 h respectively. (d-f) HeLa cells cultured in the above-mentioned groups at 72 h respectively. (g-i) HeLa cells of all groups are stained by Live/dead (green/red) kit. (j-l) Reconstruction for spatial distribution of HeLa cells by confocal imaging and z-stacking. (m-o) The X-Z section of 3D confocal images for evaluation of space for cell growth in the height direction. (p) The normalized densities of HeLa cells inside the microfluidic devices and plate after 72 h of culturing; Two-tailed unpaired Student's t-test is used for analysis of the data; *** indicate statistical significance of $P < 0.001$ ($n = 4$). (q) The viability

of HeLa cells inside the microfluidic devices and plate after 72 h of culturing; Two-tailed unpaired Student's t-test is used for analysis of the data; *** indicate statistical significance of $P < 0.001$ ($n = 4$). (r) The cell aspect ratio of all groups after 72 h of culturing; Mann-Whitney u-test is used for analysis of the data; *** indicates statistical significance of $P < 0.001$ ($n = 100$). The scale bar in (a-i) is 200 μm, and the scale bar in (j-o) is 100 μm.

HeLa cells have been cultured in the microfluidic device with 3D printing scaffold to study the biocompatibility and feasibility. Cells cultured inside the 48-well plate covered with circular glass and in the device without scaffold are used as comparisons. Fig. 6a-6c show initial condition of cells introduced into the devices and plate respectively. The states of HeLa cells were recorded within 72 h and the cells were stained by FDA/PI (green/red) after culturing for 72 h. Fig. 6d-6f show the states of HeLa cells cultured for 72 h inside the devices and plate respectively. It can be seen that the observation of HeLa cells in the chamber with scaffold is disturbed on the bright field. Hence, the live/dead (green/red) dyes of HeLa cells were merged to further estimate the cell density (as shown in Fig. 6g-6i). The changes in brightness of cells in these fluorescence images may indicate that the HeLa cells adhere to the scaffold at different depths. Fig. 6j-6l show the reconstruction for spatial distribution of HeLa cells into the device with scaffold, device without scaffold and 48-well plate respectively. Correspondingly, the X-Z sections of 3D reconstructions are shown in Fig. 6m-6o to characterize the cell distributions in the height (Z-axis) direction. It is apparently observed that the height of 3D reconstruction in the device with scaffold is greater than those in control groups. The former is approximately equal to 40 μm which is the height of the printed scaffold, whereas the latter is a monolayer under the condition of 2D culture. It is demonstrated that the 3D printing scaffold can expand the growing space in the height direction. Fig. 6p shows the normalized cell density in the device with scaffold is significantly greater than that in the control device and plate. This is because the 3D printing scaffold expands the growing space in the height direction, increasing the sites of cell attachment. Besides, the scaffold that can stabilize the flow field has the ability to weaken the effect of fluid shear stress on cells, providing a feasible microenvironment for more stable attachment of cells. These results indicate that the 3D dynamic culturing model has advantage in improving cell growth.

The cell viability of HeLa cells has been evaluated by calculating the ratio of number of live cells to number of total cells according to the results of live/dead stain. As shown in Fig. 6q, the cell viabilities in the plate and the control device are 86.7% and 90.8% respectively while it reaches 95.3% in the microfluidic device with scaffold superior to the control groups. The *t*-test results indicate that the cell viability in the device with scaffold has statistical significance compared to those in the control groups. This is not only due to an efficient process of providing fresh medium and removing of metabolic waste and dead cells inside the device, but also the sufficient growing space of cells provided by 3D printing scaffold. Moreover, the difference in cell morphology is observed in the devices and plate. Fig. 6r shows the violin plot of the cell aspect ratio in different groups after 72 h of culturing. The median of cell aspect ratios in the device with scaffold is about 3.2 which is more than 1.5-fold of that (about 2.0) in the plate and device without scaffold. Moreover, the maximum cell aspect ratio in the scaffold reaches about 8.5. These results can be explained by the regulation of cell attachment and spreading by fibronectin-coated scaffold [45]. It is demonstrated that the scaffold can promote the morphogenesis of elongated and spindle-shaped HeLa cells (Fig. S2), meaning that cellular response differs in the dynamic and 3D microenvironment from the 2D.

### 3.5. Cytotoxicity assessment of DOX in the devices and plate

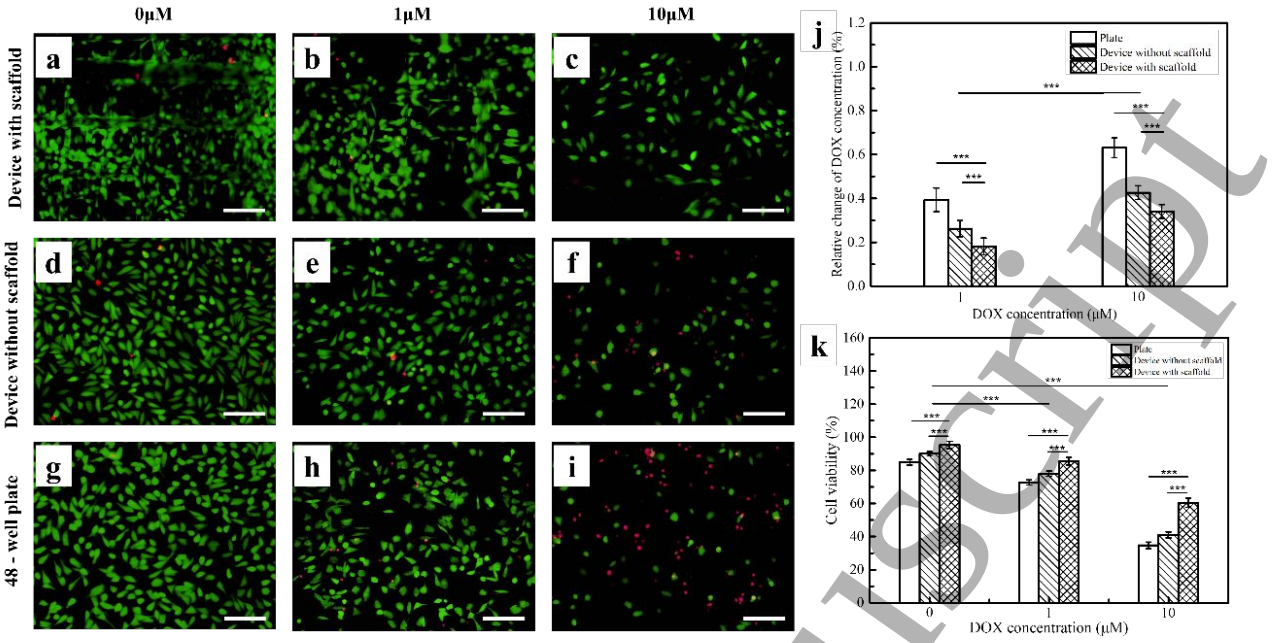


Fig. 7 HeLa cells in devices and plate after 24 h DOX treatment with different concentrations. (a-c) The live/dead fluorescence images of HeLa cells in the device with scaffold after 24 h DOX treatment with concentration of 0, 1, 10 μM. (d-f) The live/dead fluorescence images of HeLa cells in the device without scaffold after 24 h DOX treatment with concentration of 0, 1, 10 μM. (g-i) The live/dead fluorescence images of HeLa cells in the plate after 24 h DOX treatment with concentration of 0, 1, 10 μM. (j) The relative change of DOX concentration after 24 h treatment in comparison with the initial loading concentration; Two-tailed unpaired Student's t-test is used for analysis of the data; *** indicate statistical significance of $P < 0.001$ ($n = 5$). (k) The dose-dependent cell viability of all groups after 24 h treatment for cytotoxicity assessment of DOX; Two-tailed unpaired Student's t-test is used for analysis of the data; *** indicate statistical significance of $P < 0.001$ ($n = 6$). The scale bar in (a-i) is 100 μm.

The experimental results of cytotoxicity tests of DOX in our work have similar trends in comparison with previous reports [42,46,47]. Fig. 7a-7i show a dose-dependent response of HeLa cells to DOX in the devices and plate visually. Compared with the control (0 μM), most cells after 24 h treatment at 1 μM still keep live, but the number of live cells decreases observably after treatment at 10 μM. This difference in cell states is closely associated with the cellular accumulations of DOX at different concentrations. Fig. 7j shows the relative change of DOX concentration before and after treatment. It is observed that the relative change of DOX concentration in the device with scaffold is significantly different from that in the device without scaffold and plate at the same initial DOX concentration. The greater change in the plate indicates that static and homogenous treatment is more efficient in delivering DOX to cells than dynamic perfusion in the devices [42]. Besides, there is also a significant difference of this change in the same group at different initial concentrations, which is due to concentration-dependent diffusion and explains the different states of cells in Fig. 7a-7i. According to the relative change of DOX concentration and amount of consumed culture medium, the DOX accumulated in cells are calculated and shown in Fig. S3. The cellular accumulations of DOX at 10 μM are significantly more than those at 1 μM, which can explain the dose-dependent response of HeLa cells to DOX reasonably.

To assess the cytotoxicity of DOX in the devices and plate, dose-dependent viabilities of cells have been investigated by using CCK-8. As shown in Fig. 7k, the trends of cell viabilities after DOX treatment at different concentrations are consistent with those shown in the live/dead fluorescence images of HeLa cells (Fig. 7a-7i). It is observed that the cell viability in the device with scaffold is always higher than others in

the controls at different concentrations of DOX, and the cell viability decreases with the increase in DOX concentration. After treatment at 1 μM, the cell viability in the device with scaffold, device without scaffold and plate decreases about 10.3%, 13.4% and 14.3% in comparison with the control (0 μM), respectively. After treatment at 10 μM, the decrease in cell viability of these groups is about 36.6%, 54.5% and 59.1%, respectively. Higher concentration of DOX causes a more significant decrease in cell viability than the lower, which is in agreement with the above-mentioned explanation for the dose-dependent response of HeLa cells by cellular accumulation of DOX. Nevertheless, this decrease in the device with scaffold at 10 μM is smaller than that in the device without scaffold and plate. In addition to the inefficient drug delivering, an *in vivo* like microenvironment developed in the 3D scaffold may play an important role in drug resistance because the higher cell density restricts the penetration of DOX into 3D tissue-like construct [42]. The cell-cell interactions and biomechanical factors in this dynamic 3D microenvironment can also mediate the chemoresistance by inducing the expression of key proteins involved in signaling pathways [48].

Moreover, the changes in cell morphology after 24 h DOX treatment are obviously observed from fluorescence images. The cell aspect ratio was calculated to evaluate cell morphology as well. As shown in Fig. S4, the median of cell aspect ratios in each group is visibly reduced compared with that before treatment (Fig. 6r), and the median of cell aspect ratios in the device with scaffold is still higher than others. Although there are minor differences in cell morphology between treatments with different DOX concentrations, the changes in cell aspect ratios related to cellular accumulation of DOX are still obtained from the distribution of violin plot in Fig. S4. It means that this depolarizing behavior of cells after treatment also shows a dose-dependent response to DOX, which is consistent with cell viability. These results may indicate that some key proteins can be induced by DOX at different concentrations and then reorganize the cytoskeleton in various degrees, leading to the changes in cell morphology, especially cell migration ability [49,50]. Although substantial efforts are needed to apply this dynamic 3D cell culturing device to clinical trials, the *in vitro* cytotoxicity assay demonstrates that this presented device has great potential in providing native microenvironments for *in vitro* cell studies, tissue engineering and drug screening for tumor therapy indeed.

## 4. Conclusions

A " sandwich" structure-liked microfluidic device is developed for dynamic cell culture in a three-dimensional microenvironment with fluid flow. The device consists of three layers such as the upper layer being used for introducing cells and fixing scaffold, the middle scaffold layer mimicking ECM used for providing 3D attachment areas, and the bottom layer mimicking blood vessel used for supplying dynamic medium for cells. The device has been successfully fabricated using 3D printing technology and microfabrication technology. The significant consistency of results between numerical simulation and particle tracking experiment for evaluation of flow field in the device indicates that the 3D printing scaffold can provide a more stable fluid microenvironment for culturing cells. Simulations of cell culturing processes using inks with different colors indicate that the device performs well flowability. HeLa cells cultured in 3D in the microfluidic device under continuous medium supplementation demonstrate that the expanded space and steady flow field provided by scaffold indeed promotes the growth and viability of cells by comparison with these cultured in 2D in the 48-well plate and the device without scaffold. *In vitro* cytotoxicity assessment of DOX verifies that there is a higher drug resistance in the device with 3D scaffold mimicking the *in vivo* like microenvironment. The obtained results indicate that this microfluidic device with good biocompatibility and feasibility has sound potential in providing native microenvironments for *in vitro* cell studies, tissue engineering and drug screening for tumor therapy.

## Acknowledgments

This work is supported by National Natural Science Foundation of China (51875084; 51475079), the National Key R&D Program of China (2020YFB2009002, 2022YFE0199100), the Science Fund for Creative Research Groups of NSFC (51621064), the Fundamental Research Funds for the Central Universities (DUT20ZD103, DUT20YG102) and Shandong Natural Science Foundation (ZR2021QE130).

**Conflicts of interest**

There are no conflicts of interest to declare.

**References**

[1] Pattee H H 2015 Cell phenomenology: The first phenomenon *Prog. Biophys. Mol. Biol.* 119 461-468
[2] Neuzi P , Giselbrecht S, Lange K, Huang T J and Manz A 2012 Revisiting lab-on-a-chip technology for drug discovery *Future. Drug. Discov.* 11 620-632
[3] Jordan M A, Toso R J, Thrower D and Wilson L 1993 Mechanism of Mitotic Block and Inhibition of Cell Proliferation by Taxol at Low Concentrations *Proc. Natl. Acad. Scencei. U S A.* 90 9552-9556
[4] Ellingsen C, Natvig I, Gaustad J V, Gulliksrud K, Egeland T A and Rofstad E K 2009 Human cervical carcinoma xenograft models for studies of the physiological microenvironment of tumors *J. Cancer. Res.. Clin. Oncol.* 135 1177-1184
[5] Spano D and Zollo M 2012 Tumor microenvironment: a main actor in the metastasis process *Clin. Exp.. Metastas.* 29 381-395
[6] Swartz M A and Fleury M E 2007 Interstitial flow and its effects in soft tissues *Annu. Rev. Biomed. Eng.* 9 229-256
[7] Davies A E and Albeck J G 2018 Microenvironmental Signals and Biochemical Information Processing: Cooperative Determinants of Intratumoral Plasticity and Heterogeneity *Front. Cell. Dev. Biol*. 6 44-53
[8] Maia J, Caja, Strano Moraes M C, Couto N and Costa-Silva B 2018 Exosome-Based Cell-Cell Communication in the Tumor Microenvironment *Front. Cell. Dev. Biol* 6 18-27
[9] Seliktar D 2012 Designing cell-compatible hydrogels for biomedical applications *Science* 336 1124-1128
[10] Edmondson R, Broglie J J, Adcock A F and Yang L 2014 Three-Dimensional Cell Culture Systems and Their Applications in Drug Discovery and Cell-Based Biosensors *Assay. Drug. Dev. Techn.* 12 207-218
[11] Geckil H, Xu F, Zhang X, Moon S and Demirci U 2010 Engineering hydrogels as extracellular matrix mimics *Nanomedicine.* 5 469-484
[12] Tibbitt M W and Anseth K S 2009 Hydrogels as extracellular matrix mimics for 3D cell culture *Biotechnol. Bioeng.* 103 655-663
[13] Aamodt J M and Grainger D W 2016 Extracellular matrix-based biomaterial scaffolds and the host response *Biomaterials* 86 68-82
[14] Chen, Ming Fa and Liu X 2016 Advancing biomaterials of human origin for tissue engineering *Prog. Polym. Science.* 53 83-168
[15] Huang G, Li F, Zhao X, Ma Y, Li Y and Lin M et al 2017 Functional and Biomimetic Materials for Engineering of the Three-Dimensional Cell Microenvironment *Chem. Rev.* 117 12764-12850
[16] Ford M C, Bertram J P, Hynes S R, Michaud M, Li Q, Young M, Segal S S, Madri J A and Lavik E B 2006 A Macroporous Hydrogel for the Coculture of Neural Progenitor and Endothelial Cells to Form Functional Vascular Networks *in vivo Proc. Natl. Acad. Science. USA* 103 2512-2517
[17] Donius A E, Liu A, Berglund L A and Wegst U G K 2014 Superior mechanical performance of highly porous anisotropic nanocellulose–montmorillonite aerogels prepared by freeze casting *J. Mech. Behav. Biomed. Mater.* 37 88-99

[18] Ho M, Kuo P, Hsieh H, Hsien T, Hou L, Lai J and Wang D 2004 Preparation of porous scaffolds by using freeze-extraction and freeze-gelation methods *Biomaterials* 25 129-138
[19] Ji C, Annabi N, Hosseinkhani M, Sivaloganathan S and Dehghani F 2012 Fabrication of poly-DL-lactide/polyethylene glycol scaffolds using the gas foaming technique *Acta. Biomater.* 8 570-578
[20] He J, Xia P and Li D 2016 Development of melt electrohydrodynamic 3D printing for complex microscale poly (ε-caprolactone) scaffolds *Biofabrication* 8 35008
[21] Zhang and Shrike Yu et al 2016 Bioprinting 3D Microfibrous Scaffolds for Engineering Endothelialized Myocardium and Heart-on-a-Chip *Biomaterials* 110 45-59
[22] Tan Z, Liu T, Zhong J, Yang Y and Tan W 2017 Control of cell growth on 3D-printed cell culture platforms for tissue engineering *J. Biomed. Mater. Res. A.* 105 3281-3292
[23] Hugo Domejean et al 2016 Controlled production of sub-millimeter liquid core hydrogel capsules for parallelized 3D cell culture *Lab. Chip.* 17 110-119
[24] Parrilla-Gutierrez J M, Tsuda S, Grizou J, Taylor J, Henson A and Cronin L 2017 Adaptive artificial evolution of droplet protocells in a 3D-printed fluidic chemorobotic platform with configurable environments *Nat. Commun.* 8 1144-1153
[25] Van Duinen and Vincent et al 2015 Microfluidic 3D cell culture: from tools to tissue models *Curr. Opin. Biotechnol.* 35 118-126
[26] Liu W, Sun M, Lu B, Yan M, Han K and Wang J 2019 A microfluidic platform for multi-size 3D tumor culture, monitoring and drug resistance testing *Sens. Actuators. B. Chem.* 292 111-120
[27] Chang H, Lin C, Juang D, Wu H, Lee C, Chen C and Hsu C 2019 Multilayer architecture microfluidic network array for combinatorial drug testing on 3D-cultured cells *Biofabrication* 11 35024
[28] Chen Y, Gao D, Liu H, Lin S and Jiang Y 2015 Drug cytotoxicity and signaling pathway analysis with three-dimensional tumor spheroids in a microwell-based microfluidic chip for drug screening *Anal Chim. Acta.* 898 85-92
[29] Ziolkowska K, Stelmachowsk A a, Kwapiszewski R, Chudy M, Dybko A and Brzozka Z 2013 Long-term three-dimensional cell culture and anticancer drug activity evaluation in a microfluidic chip *Biosens. Bioelectron* 40 68-74
[30] Knowlton S, Yu C H, Ersoy F, Emadi S, Khademhosseini A and Tasoglu S 2016 3D-printed microfluidic chips with patterned, cell-laden hydrogel constructs *Biofabrication* 8 25019
[31] Li Y, Zhang T, Pang Y, Li L, Chen Z and Sun W 2019 3D bioprinting of hepatoma cells and application with microfluidics for pharmacodynamic test of Metuzumab *Biofabrication* 11 34102
[32] Bhise N, Manoharan V, Massa S, Tamayol A, Ghaderi M, Miscuglio M, Lang Q and Zhang Y et al 2016 A liver-on-a-chip platform with bioprinted hepatic spheroids *Biofabrication* 8 014101
[33] Toh Y, Lim T, Tai D, Xiao G, Noort D and Yu H 2009 A microfluidic 3D hepatocyte chip for drug toxicity testing *Lab. Chip.* 9 2026-2035
[34] Fang Y, Zhang T, Zhang L, Gong W and Sun W 2019 Biomimetic design and fabrication of scaffolds integrating oriented micro-pores with branched channel networks for myocardial tissue engineering *Biofabrication* 11 35004
[35] Baker and Brendon M et al 2013 Microfluidics embedded within extracellular matrix to define vascular architectures and pattern diffusive gradients *Lab. Chip.* 16 3246
[36] Miller J S, Stevens K R, Yang M T, Baker B M, Nguyen D T and Cohen D M et al 2012 Rapid casting of patterned vascular networks for perfusable engineered three-dimensional tissues *Nat. Mater.* 11 768-774
[37] Li J, Wei J, Liu Y, Liu B, Liu T, Jiang Y, Ding L and Liu C 2017 A microfluidic design to provide a stable and uniform *in vitro* microenvironment for cell culture inspired by the redundancy characteristic of

leaf areoles *Lab. Chip.* 17 3921-3933
[38] Wei J, Liu C, Jiang Y, Duan C, Chen L, Li W, Liu B and Li J 2019 Microfluidic device for generating regionalized concentration gradients under a stable and uniform fluid microenvironment *J. Micromech. Microeng.* 29 15008
[39] Li K, Wang D, Wang Q, Song K, Liang J, Sun Y and Madoua M 2018 Thermally Assisted Electrohydrodynamic Jet Hig-Resolution Printing of High-Molecular Weight Biopolymer 3D Structures *Macromol. Mater. Eng.* 303 1800345
[40] Moroni L, Wijn J R de and Blitterswijk C A van 2006 3D fiber-deposited scaffolds for tissue engineering: Influence of pores geometry and architecture on dynamic mechanical properties *Biomaterials* 27 974-985
[41] Sell S, Barnes C, Simpson D and Bowlin G 2008 Scaffold permeability as a means to determine fiber diameter and pore size of electrospun fibrinogen *J. Biomed. Mater. Res. A.* 85A 115-126
[42] Yang Y, Liu S, Chen C, Huang H, Tao L, Qian Z and Li W 2020 Microfluidic-enabled self-organized tumor model for in vitro cytotoxicity assessment of doxorubicin *Biomed. Microdevices* 22 70
[43] Yokochi T and Robertson K 2004 Doxorubicin inhibits DNMT1, resulting in conditional apoptosis *Mol. Pharmacol.* 66 1415-1420
[44] Li Z, Li H, Liu B, Luo J, Qin X and Gong M et al 2020 Inhibition of miR-25 attenuates doxorubicin-induced apoptosis, reactive oxygen species production and DNA damage by targeting PTEN *Int. J. Med. Sci.* 17 1415-1427
[45] Ye W, Xie C, Liu Y, He Y, Gao Q and Ouyang A 2020 3D printed high-resolution scaffold with hydrogel microfibers for providing excellent biocompatibility *J. Biomater. Appl.* 0 1-10
[46] Lovitt C, Shelper T and Avery V 2018 Doxorubicin resistance in breast cancer cells is mediated by extracellular matrix proteins *BMC Cancer* 18 41
[47] Prince E, Kheiri S, Wang Y, Xu F, Cruickshank J and Topolskaia V et al 2022 Microfluidic Arrays of Breast Tumor Spheroids for Drug Screening and Personalized Cancer Therapies *Adv. Healthcare Mater.* 11 2101085
[48] Nwosu Z, Pioronska W, Battello N, Zimmer A, Dewidar B, Han M and Pereira S et al Severe metabolic alterations in liver cancer lead to ERK pathway activation and drug resistance *EBioMedicine* 54 102699
[49] Zhang G, Huang L, Wu J, Liu Y, Zhang Z and Guan Q 2020 Doxorubicin-loaded folate-mediated pH-responsive micelle based on Bletilla striata polysaccharide: Release mechanism, cellular uptake mechanism, distribution, pharmacokinetics, and antitumor effects *Int. J. Biol. Macromol.* 164 566-577
[50] Kan L, Smith A, Chen M, Ledford B, Fan H, Liu Z and He J 2016 Rho-Associated Kinase Inhibitor (Y-27632) Attenuates Doxorubicin-Induced Apoptosis of Human Cardiac Stem Cells *Plos One* 10 e0144513